



PHOTONICS Research

Augmenting photoluminescence of monolayer MoS₂ using high order modes in a metal dimer-on-film nanocavity

SHIYIN CAO,¹ LIPING HOU,¹ QIFA WANG,¹ CHENYANG LI,¹ WEIXING YU,² XUETAO GAN,^{1,5} KAIHUI LIU,³ MALIN PREMARATNE,⁴  FAJUN XIAO,^{1,2,6}  AND JIANLIN ZHAO^{1,7} 

¹MOE Key Laboratory of Material Physics and Chemistry under Extraordinary Conditions, and Shaanxi Key Laboratory of Optical Information Technology, School of Physical Science and Technology, Northwestern Polytechnical University, Xi'an 710129, China

²Key Laboratory of Spectral Imaging Technology of Chinese Academy of Sciences, Xi'an 710119, China

³State Key Laboratory for Mesoscopic Physics, Collaborative Innovation Centre of Quantum Matter, School of Physics, Peking University, Beijing 100871, China

⁴Advanced Computing and Simulation Laboratory (A_χL), Department of Electrical and Computer Systems Engineering, Monash University, Clayton, VIC 3800, Australia

⁵e-mail: xuetaogan@nwpu.edu.cn

⁶e-mail: fxiao@nwpu.edu.cn

⁷e-mail: jlzhao@nwpu.edu.cn

Received 10 November 2020; revised 26 January 2021; accepted 1 February 2021; posted 2 February 2021 (Doc. ID 414613); published 22 March 2021

Plasmonic particle-on-film nanocavities, supporting gap modes with ultra-small volume, provide a great solution to boost light–matter interactions at the nanoscale. In this work, we report on the photoluminescence (PL) enhancement of monolayer MoS₂ using high order modes of an Au nanosphere dimer-on-film nanocavity (DoFN). The high order plasmon modes, consisting of two bonding quadrupoles in the dimer and their images in the Au film, are revealed by combining the polarization-resolved scattering spectra with the numerical simulations. Further integrating the monolayer MoS₂ into the DoFN, these high order modes are used to enhance PL intensity through simultaneously boosting the absorption and emission processes, producing a 1350-fold enhancement factor. It opens an avenue to enhance the light–matter interaction with high order plasmon modes and may find applications in future optoelectronics and nanophotonics devices. © 2021 Chinese Laser Press

<https://doi.org/10.1364/PRJ.414613>

1. INTRODUCTION

Plasmonic nanostructures show unprecedented ability to confine light in subwavelength volume due to the surface plasmons they support. This peculiar feature is responsible for a plethora of enhanced optical processes, including surface-enhanced Raman scattering [1], photoemission [2], nonlinear optics [3], and nanolasing [4,5]. To achieve a strong light–matter interaction in aforementioned phenomena, it is essential to carefully mold plasmonic nanostructures. For example, optimizing the patterned metallic structures can align the plasmon resonances with the absorption and/or emission bands of the monolayer MoS₂ atop that produce strong and well-manipulated plasmon–exciton interactions and promise high-efficiency and ultrafast optoelectronic applications [6–9]. Also, recently, it has been demonstrated that the Anderson localization resulting from an increasing of the disorder in silver nanoarrays is possible to further squeeze the localized surface plasmon, giving rise to a substantially enhanced photoluminescence (PL) of

dye molecules [10]. With the advance of nanofabrication and colloidal approaches, plasmonic nanostructures with a small feature/gap size can be readily prepared as exemplified by the crescent-ring [11], bowtie antenna [12], and Au nanosphere dimer [13], allowing for confining light down to tens of nanometers to probe novel light–matter interactions. However, further scaling the light confinement volume requires controlling the structure feature/gap size with nanometer accuracy, presenting a tremendous challenge even for state-of-the-art lithographic and colloidal methods. A promising solution is integrating the sharp metallic protrusion into a scanning probe microscopy, such as a tip-enhanced spectroscopy (TES) configuration. This enables an extreme confinement of light with the nanometric mode volume, rendering a PL enhancement of three orders for the monolayer MoS₂ [14].

Alternatively, the rapidly growing metal particle-on-film nanocavity [15–19], composed of a closely spaced nanoparticle and metal film, provides an up-and-coming solution to squeeze

light in the true nanometer or even subnanometer region. For example, using thin film deposition technology and the bottom-up process, the spacer between the Au nanosphere and metal film can be well tuned with the precision of a few angstroms, yielding a field enhancement factor of over 10^3 [15]. This intriguing property not only facilitates the observations of exciting phenomena including strong coupling [20–22] and quantum tunneling [23], but also enables fascinating applications in hyper-spectral imaging [24], nanoscale sensing [25], and switching [26]. More importantly, benefitting from the bottom-up process, it is much more convenient to precisely place the active media (e.g., molecules [27], quantum dots [28], and two-dimensional materials [29]) in the nanogaps, making the single-molecule-level light–matter interactions possible.

Monolayer molybdenum disulfide (MoS_2) is an appealing building block for future nanophotonics and optoelectronics devices relying on its intriguing optical properties [30,31]. However, for practical application, it is highly needed to enhance its intrinsically low absorption [32] and small PL quantum yield [33]. Recently, Au nanosphere dimer-on-film nanocavities (DoFNs) have been demonstrated to be the ideal platform for realizing strong light–matter interactions, owing to their wealth of plasmon modes resulting from particle–particle and particle–film couplings [34,35]. Recently, a large number of experimental studies have paid attention to PL enhancement using the dipole or coupled dipole modes of DoFNs [18,36]. However, relying on high order modes is scarce, as their dark-mode nature possesses a much stronger electric field enhancement. In this work, we fabricate Au nanosphere DoFNs with a single-particle diameter of 140 nm. The polarization-resolved scattering spectra of DoFNs reveal the film-coupled bonding quadrupole modes. These modes allow us to simultaneously boost the absorption and emission processes of the monolayer MoS_2 , achieving a 1350-fold PL enhancement.

2. EXPERIMENTAL AND SIMULATION DETAILS

The Au nanosphere DoFNs were fabricated using the bottom-up self-assembly technique. Specifically, a 50-nm-thick Au substrate with atomic flatness was prepared via thermal evaporation at a deposition rate of $1 \text{ \AA}/\text{s}$ ($1 \text{ \AA} = 0.1 \text{ nm}$) followed by a template-stripping method [37]. Then, to avoid PL quenching, an Al_2O_3 spacer layer with a thickness of 6 nm was deposited on the Au substrate by the atomic layer deposition technique. The monolayer MoS_2 was mechanically exfoliated from bulk crystal (HQ-graphene, Inc.), and then deterministically transferred onto the Al_2O_3 layer with the help of a polydimethylsiloxane gel-film. Finally, 140-nm-diameter Au nanospheres (Nanoseedz, Inc.), coated with a 2 nm cetyltrimethylammonium bromide surfactant polymer, were drop-cast on the monolayer MoS_2 and blow-dried in air for seconds to form nanosphere dimers.

In our measurement, the dark-field images and scattering spectra of the DoFNs are characterized using a home-built dark-field confocal microscope [38], where a polarization-controlled white light from a halogen lamp is obliquely illuminated on the sample through a $20\times$ objective (Mitutoyo, NA 0.4) at an incident angle of 60° . The scattering light is collected with

an upright $50\times$ objective (Nikon NA 0.6), and then recorded as the dark image and scattering spectrum by a CCD camera and an imaging spectrometer (Andor Shamrock SR-500i), respectively. The PL measurement was carried out on the same confocal microscope. A He–Ne laser beam (wavelength at 633 nm) with a power of $\sim 0.4 \text{ mW}$ is focused on the sample through a $150\times$ objective (Leica, NA 0.9). The diameter of the focused excitation beam is estimated to be $\sim 1 \text{ }\mu\text{m}$ in the sample plane. The backscattered PL emission is collected by the same objective. After passing through a long-pass filter, the collected emission is delivered to the spectrometer for spectral analysis. Notice that the dimer with a separation at least $2 \text{ }\mu\text{m}$ away from other nanosphere clusters and the MoS_2 edge was deliberately selected by spatially filtering optical signals through a pinhole, to avoid the unwanted scattering and PL contributions.

The optical responses of a plasmonic nanocavity are calculated by a full-wave simulation based on the finite element method (FEM). The structural configurations are modeled as the true values of the fabricated system. The permittivity of Au is taken from the experimental data of Johnson and Christy [39]. The refractive index of the Al_2O_3 layer is taken as a constant of 1.5. The permittivity of monolayer MoS_2 is modeled by the experimental data of Jung *et al.* [40]. The scattering field is calculated by a two-step method, where the background field, derived from the plane wave incident on the bare substrate, is used as the excitation with the Au dimer present. The scattered field of each wavelength is collected within a cone of half-angle 37° based on the numerical aperture of the objective to arrive at the scattering spectrum. The charge distribution of the plasmonic nanocavity is obtained by calculating the difference of the normal component of the electric field above and below the metal surface according to Gauss's law [41].

The quantum yield enhancement of the nanocavity coupled MoS_2 was calculated with the finite-difference time domain method, where the monolayer MoS_2 was set as a monochromatic dipole with a horizontal orientation. We calculated the dyadic Green's function of the hybrid system by varying the dipole position on a discrete grid (26×18) beneath the dimer [42]. The radiative and non-radiative decay rates were obtained by integrating the power radiated out of the hybrid system and absorbed by the DoFN, respectively.

3. RESULTS AND DISCUSSION

The Au nanosphere DoFN is schematically shown in Fig. 1(a), where the dimer and ultrasmooth Au film are separated by the Al_2O_3 spacer and monolayer MoS_2 flake. The bright- and dark-field images of this plasmonic nanocavity are, respectively, displayed in Figs. 1(b) and 1(c), where the Au dimer is marked within the white box. The Au nanosphere radius is $\sim 70 \text{ nm}$ measured by the scanning electron microscope (SEM), as shown in Fig. 1(d). The dark yellow section in Fig. 1(b) presents the exfoliated MoS_2 monolayer flake, which has a dimension over $30 \text{ }\mu\text{m}$. The layer number of this MoS_2 flake is further confirmed by the Raman spectrum carried out on a commercial confocal microscope (WITec, Alpha 300R) as shown in Fig. 1(e), where the in-plane mode E_{2g}^1 and the out-of-plane mode A_{1g} have a separation of 18 cm^{-1} , agreeing with the typical mode interval in the monolayer MoS_2 [43].

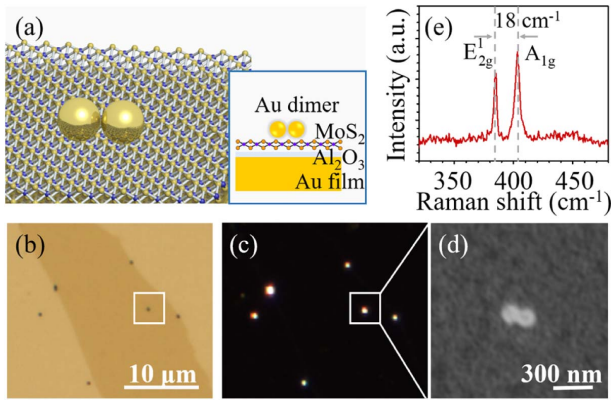


Fig. 1. (a) Schematic of Au nanosphere dimer-on-film nanocavity (DoFN) composed of the Au nanosphere dimer and Au film spaced by the monolayer MoS₂ and Al₂O₃. (b) Bright- and (c) dark-field images of the Au dimer DoFNs. The white boxes denote the Au dimer measured in the optical setups. (d) SEM image of the DoFN. (e) Raman spectrum of the monolayer MoS₂ taken nearby the dimer.

Film-coupled dimers offer an ideal platform to facilitate strong plasmon hybridization, resulting in extremely pronounced enhancements for both electric and magnetic fields in the gap region. We then record the polarization-resolved scattering spectra to analyze the hybridized modes residing in the DoFNs. Two typical excitation configurations are adopted where the wave vectors (\mathbf{k}) of the illumination are perpendicular to the long (configuration 1) and short axes of the dimer (configuration 2), as shown in the inset of Figs. 2(a), 2(b) and 2(c), 2(d), respectively. It can be found in Figs. 2(a) and 2(b) that strong scattering peaks centered around 650 and 740 nm are, respectively, excited by s- and p-polarized beams under configuration 1. In configuration 2, predominant peaks appear at wavelengths of 750 and 640 nm when the illuminations are s- and p-polarized beams as shown in Figs. 2(c) and 2(d), respectively. These scattering peaks are well reproduced by FEM simulations, as shown in the solid lines in the right panels of Fig. 2. Compared to the experimental results, apparent discrepancies are found in the simulated scattering spectrum excited by the s-polarized beam under configuration 1, which shows a peak around 560 nm and a mode beyond the wavelength of 750 nm. The reasons are that nanospheres of the dimer are slightly elliptical [see Fig. 1(d)], and the side illumination is focused by the objective with NA = 0.4, which broadens the incident angle range from 36.4° to 83.5°. The simulation for a better fitting of the experiment can be achieved by setting the nanosphere radius with deviations of ± 2 nm along two principal axes and an incident angle of 80°.

To unravel the origin of scattering peaks observed in Fig. 2, we calculate the transient surface charge distributions of the DoFNs. According to the charge distributions, we distinguish all the mode types within the whole spectral range and decompose the scattering spectra with multiple Lorentzian functions, as shown by the dashed lines in the right panels of Fig. 2. Here, we focus mainly on the spectral range of PL emission of MoS₂ and label the modes in this range as I–VI, whose charge distributions are displayed in the upper panels of Fig. 3. As

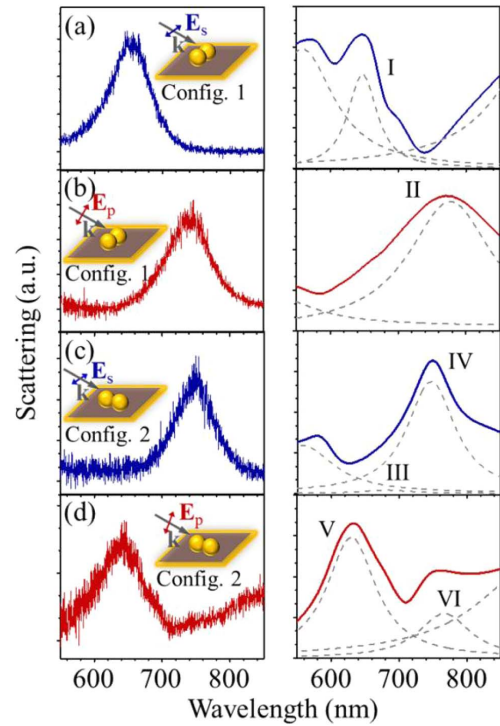


Fig. 2. (a)–(d) Scattering spectra of Au nanosphere DoFNs illuminated with two typical wave vectors and polarizations shown in the insets of left panels. Here, the left and right panels are for the experiment and simulation results, respectively.

can be seen in Fig. 3(a), mode I ($\lambda = 648$ nm) is characterized by a film-coupled longitudinal bonding quadrupole mode (LBQ) due to the strong interparticle coupling resulting from

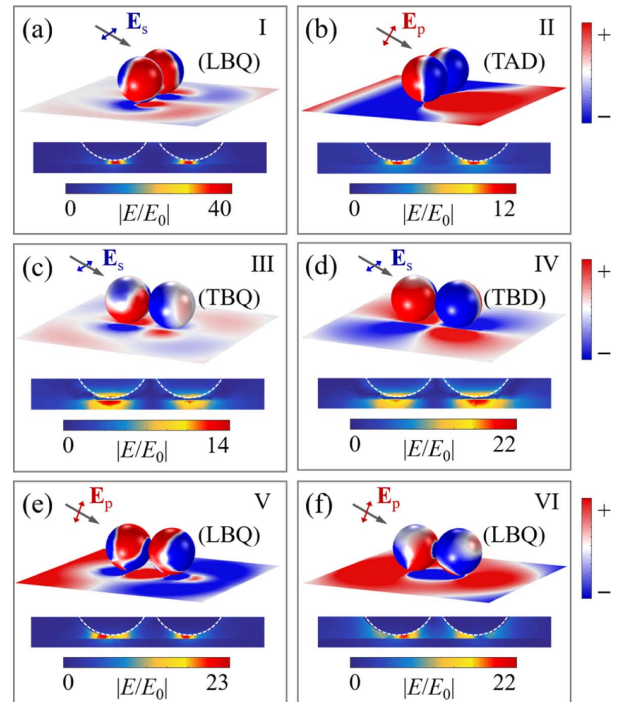


Fig. 3. (a)–(f) Charge distributions (upper panels) and electric field enhancement maps (lower panels) of modes I–VI shown in Fig. 2.

the s-polarized beam under configuration 1. Mode II ($\lambda = 776$ nm), shown in Fig. 3(b), is assigned to be a film-coupled transverse antibonding dipole mode (TAD). Of note is that in this scenario, the dipole moment of each monomer is distorted due to the considerable vertical electric field component of the excitation. For configuration 2, the symmetry of two monomers with regard to the \mathbf{k} vector is broken, introducing an obvious phase retardation effect across the dimer. As a result, under s-polarized beam excitation, modes III ($\lambda = 680$ nm) and IV ($\lambda = 749$ nm) are featured with out-of-phase coupling in two monomers and are denoted as the film-coupled transverse bonding quadrupole mode (TBQ) and dipole mode (TBD) as shown in Figs. 3(c) and 3(d), respectively. In addition, compared with TBD, TBQ has a smaller net dipole moment, rendering lower coupling efficiency with the excitation and a lower scattering radiation, as seen in the left panel of Fig. 2(c). On the other hand, as the excitation is a p-polarized beam, the strong interparticle coupling produces modes V ($\lambda = 630$ nm) and VI ($\lambda = 767$ nm), the two LBQs shown in Figs. 3(e) and 3(f), respectively. For these two LBQs, the quadrupole modes in two monomers are distorted with different orientations due to the vertical electric field component of the excitation and the phase retardation effect, distinguished from mode I, which is composed of two identical quadrupole modes. It is also worth noting that compared to those of modes I and V, LBQ of mode VI is a lower order mode, as evidenced by the less-charged nodal lines on the Au film.

The lower panels of Fig. 3 display the electric field enhancement maps in the nanocavity gap region. It is apparent that the hybridized quadrupole modes, such as LBQs, produce a stronger local field than the hybridized dipolar ones (TBD, TAD) due to their dark-mode nature. In free space, the excitation rate of PL γ_{ex}^0 is determined by the interaction between the transition dipole moment of MoS₂ \mathbf{p} and incident electric field \mathbf{E}_0 , following $|\mathbf{p} \cdot \mathbf{E}_0|^2$. As seen in Fig. 3, the strong local field produced by the hybridized quadrupole modes could result in an over two orders of enhanced excitation rate ($\gamma_{\text{ex}}/\gamma_{\text{ex}}^0 \propto |\mathbf{E}|^2/|\mathbf{E}_0|^2$). Also, these hybridized quadrupole modes are capable of accelerating the spontaneous emission rate of the MoS₂ nearby, with a quantum yield given by $QY = \gamma_r/(\gamma_r + \gamma_{\text{nr}} + \gamma_{\text{int}}^0)$ [42]. Here, γ_{int}^0 is the intrinsic nonradiative decay rate of MoS₂, and γ_r and γ_{nr} are radiative and nonradiative decay rates of MoS₂ in the presence of nanocavity, respectively. The inset of Fig. 4(a) displays the enhanced quantum yield of nanocavity coupled MoS₂ at 685 nm. An eight-fold quantum yield enhancement is found compared to that of the monolayer MoS₂ on the quartz substrate ($QY_0 = 0.35\%$). Therefore, to fully use the substantial field enhancement of these hybridized quadrupole modes, we choose the PL excitation wavelength as 633 nm, close to the resonance peak of LBQs, to simultaneously boost the PL absorption and emission processes of the monolayer MoS₂. The PL spectrum taken from a MoS₂ region with the dimer is shown in Fig. 4(a), where the red and blue curves are the polarization of the excitation along and perpendicular to the dimer axis, respectively. Notably, as strong plasmon resonances also produce an enhanced PL of DoFN itself, we subtract this additional PL intensity from the enhanced PL spectra of MoS₂ shown in Fig. 4(a). It can

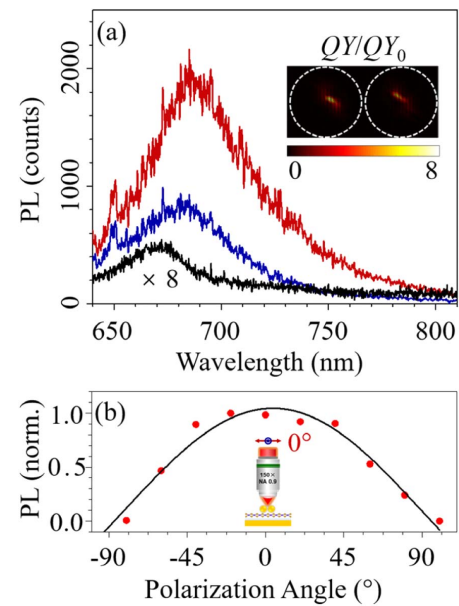


Fig. 4. (a) Photoluminescence (PL) spectra of MoS₂ around the DoFNs (red and blue curves for polarization along and perpendicular to dimer axis, respectively) and on bare Au film (black curve with 8× magnification). (b) Polarization dependence of the PL peak intensity. Insets in (a) and (b) are the quantum yield enhancement at 685 nm and PL excitation configuration, respectively.

be seen that the PL intensity is significantly enhanced compared to the background PL without the dimer [black curve in Fig. 4(a)], showing maximum enhancements of 32- and 14-fold for two orthogonal polarizations. Considering that the beam size of PL excitation is much larger than the dimer, the enhanced PL intensity is contributed from both the region around the dimer and the background MoS₂. To extract the real PL enhancement around the dimer, we define the PL enhancement factor as [44]

$$EF = \frac{I_{\text{dim}} - I_0 - I_{\text{dim}0}}{I_0} \frac{S_0}{S_{\text{dim}}}, \quad (1)$$

where $I_{\text{dim}0}$, I_{dim} , and I_0 are the PL intensities from the DoFN only, MoS₂ area with the dimer, and the background MoS₂, respectively. S_0 denotes the excitation area on MoS₂ ($\sim 0.78 \mu\text{m}^2$), and S_{dim} represents the area of the dimer ($\sim 0.03 \mu\text{m}^2$). After evaluation by Eq. (1), the maximum PL enhancement factor is found to be ~ 1350 for the polarization along the dimer axis and a value of ~ 570 for the polarization perpendicular to the dimer axis.

The difference in enhancement factors between two orthogonal polarizations can be attributed to the plasmonic modes participating in PL enhancement. When the polarization is along the dimer axis, the tightly focused PL excitation can be decomposed into the s-polarized beam of configuration 1 and p-polarized beam of configuration 2. Therefore, it excites modes I, V, and VI to enhance the PL of MoS₂. For the polarization perpendicular to the dimer axis, the PL excitation can be regarded as the p-polarized beam of configuration 1 and s-polarized beam of configuration 2, which excite modes II–IV to boost the PL. As seen in the lower panels of Fig. 3, modes I,

V, and VI produce overall stronger field enhancement than modes II–IV. Additionally, modes I and V are more in resonance with the PL excitation, eventually contributing to a larger PL enhancement factor when the polarization is along the dimer axis. Thus, we evaluate the PL enhancement for two orthogonal polarizations by [42]

$$EF(r) = \frac{\eta \gamma_{ex}(r)}{\eta_0 \gamma_{ex}^0} \cdot \frac{QY(r)}{QY_0}, \quad (2)$$

where η and η_0 are the PL collection efficiencies for the MoS₂ embedded in the nanocavity and on the quartz substrate, respectively. Note that the PL of monolayer MoS₂ is dominated by the in-plane transition dipole [45]; only in-plane electric components have considerable interaction with the emission dipole of MoS₂ and are considered in the PL estimation. After integrating EF in Eq. (2) within the projection area of the dimer, it yields the maximum PL enhancement factor ratio of 2.04 between two orthogonal polarizations, which is in coincidence with the value of 2.37 derived from the experiment. Also, we examine the polarization-dependent PL intensity of MoS₂ embedded in DoFNs, as shown in Fig. 4(b), which can be well described by a cosine function [solid line in Fig. 4(b)] with maximum and minimum values for the polarization along and perpendicular to the dimer axis, respectively. This further confirms the PL enhancement is contributed mainly from modes I and V.

4. CONCLUSION

In summary, we have fabricated a particle-on-film nanocavity composed of the Au nanosphere dimer and ultra-smooth Au film. The polarization-resolved scattering spectra uncover a high order plasmon mode of the nanocavity. Further full-wave simulations confirm these modes are attributed to two longitudinal bonding quadrupoles of the dimer coupled with their images in the Au film. By integrating the monolayer MoS₂ into the nanocavity, we demonstrate these high order modes can enhance the PL intensity of MoS₂ through boosting both the absorption and emission processes, leading to a 1350-fold enhancement factor. Our results pave the way for exploiting high order plasmon modes to enhance light–matter interactions at the nanoscale and have potential applications in future optoelectronics and nanophotonics devices such as light-emitting diodes, photovoltaics, and photodetectors.

Funding. National Key Research and Development Program of China (2017YFA0303800); National Natural Science Foundation of China (11634010, 11874050, 61675170); Open Research Fund of CAS Key Laboratory of Spectral Imaging Technology (LSIT201913W); Fundamental Research Funds for the Central Universities (310201911fz049, 3102019JC008).

Acknowledgment. The authors acknowledge the SEM measurements by the Analytical and Testing Center of Northwestern Polytechnical University.

Disclosures. The authors declare no conflicts of interest.

REFERENCES

- H. X. Xu, E. J. Bjerneld, M. Kall, and L. Borjesson, "Spectroscopy of single hemoglobin molecules by surface enhanced Raman scattering," *Phys. Rev. Lett.* **83**, 4357–4360 (1999).
- R. Bormann, M. Gulde, A. Weismann, S. V. Yalunin, and C. Ropers, "Tip-enhanced strong-field photoemission," *Phys. Rev. Lett.* **105**, 147601 (2010).
- J. Lee, M. Tymchenko, C. Argyropoulos, P. Y. Chen, F. Lu, F. Demmerle, G. Boehm, M. C. Amann, A. Alu, and M. A. Belkin, "Giant nonlinear response from plasmonic metasurfaces coupled to intersubband transitions," *Nature* **511**, 65–69 (2014).
- R. F. Oulton, V. J. Sorger, T. Zentgraf, R. M. Ma, C. Gladden, L. Dai, G. Bartal, and X. Zhang, "Plasmon lasers at deep subwavelength scale," *Nature* **461**, 629–632 (2009).
- M. Premaratne and M. I. Stockman, "Theory and technology of SPASERS," *Adv. Opt. Photon.* **9**, 79–128 (2017).
- S. Najmaei, A. Mlayah, A. Arbouet, C. Girard, J. Leotin, and J. Lou, "Plasmonic pumping of excitonic photoluminescence in hybrid MoS₂-Au nanostructures," *ACS Nano* **8**, 12682–12689 (2014).
- Y. Yu, Z. Ji, S. Zu, B. Du, Y. Kang, Z. Li, Z. Zhou, K. Shi, and Z. Fang, "Ultrafast plasmonic hot electron transfer in Au nanoantenna/MoS₂ heterostructures," *Adv. Funct. Mater.* **26**, 6394–6401 (2016).
- W. Lin, Y. Shi, X. Yang, J. Li, E. Cao, X. Xu, T. Pullerits, W. Liang, and M. Sun, "Physical mechanism on exciton-plasmon coupling revealed by femtosecond pump-probe transient absorption spectroscopy," *Mater. Today Phys.* **3**, 33–40 (2017).
- W.-B. Shi, L. Zhang, D. Wang, R.-L. Zhang, Y. Zhu, L.-H. Zhang, R. Peng, W. Bao, R.-H. Fan, and M. Wang, "Hybrid coupling enhances photoluminescence of monolayer MoS₂ on plasmonic nanostructures," *Opt. Lett.* **43**, 4128–4131 (2018).
- Y. Zhu, H. Jing, R.-W. Peng, C.-Y. Li, J. He, B. Xiong, and M. Wang, "Realizing Anderson localization of surface plasmon polaritons and enhancing their interactions with excitons in 2D disordered nanostructures," *Appl. Phys. Lett.* **116**, 201106 (2020).
- A. Aubry, D. Y. Lei, A. I. Fernandez-Dominguez, Y. Sonnefraud, S. A. Maier, and J. B. Pendry, "Plasmonic light-harvesting devices over the whole visible spectrum," *Nano Lett.* **10**, 2574–2579 (2010).
- J. Merlein, M. Kahl, A. Zuschlag, A. Sell, A. Halm, J. Boneberg, P. Leiderer, A. Leitenstorfer, and R. Bratschkitsch, "Nanomechanical control of an optical antenna," *Nat. Photonics* **2**, 230–233 (2008).
- C. E. Talley, J. B. Jackson, C. Oubre, N. K. Grady, C. W. Hollars, S. M. Lane, T. R. Huser, P. Nordlander, and N. J. Halas, "Surface-enhanced Raman scattering from individual Au nanoparticles and nanoparticle dimer substrates," *Nano Lett.* **5**, 1569–1574 (2005).
- L. Meng and M. Sun, "Tip-enhanced photoluminescence spectroscopy of monolayer MoS₂," *Photon. Res.* **5**, 745–749 (2017).
- C. Ciraci, R. T. Hill, J. J. Mock, Y. Urzhumov, A. I. Fernandez-Dominguez, S. A. Maier, J. B. Pendry, A. Chilkoti, and D. R. Smith, "Probing the ultimate limits of plasmonic enhancement," *Science* **337**, 1072–1074 (2012).
- G. M. Akselrod, C. Argyropoulos, T. B. Hoang, C. Ciraci, C. Fang, J. Huang, D. R. Smith, and M. H. Mikkelsen, "Probing the mechanisms of large Purcell enhancement in plasmonic nanoantennas," *Nat. Photonics* **8**, 835–840 (2014).
- H. Harutyunyan, A. B. F. Martinson, D. Rosenmann, L. K. Khorashad, L. V. Besteiro, A. O. Govorov, and G. P. Wiederrecht, "Anomalous ultrafast dynamics of hot plasmonic electrons in nanostructures with hot spots," *Nat. Nanotechnol.* **10**, 770–775 (2015).
- G. C. Li, Y. L. Zhang, J. Jiang, Y. Luo, and D. Y. Lei, "Metal-substrate-mediated plasmon hybridization in a nanoparticle dimer for photoluminescence line-width shrinking and intensity enhancement," *ACS Nano* **11**, 3067–3080 (2017).
- J. Shi, Y. Li, M. Kang, X. He, N. J. Halas, P. Nordlander, S. Zhang, and H. Xu, "Efficient second harmonic generation in a hybrid plasmonic waveguide by mode interactions," *Nano Lett.* **19**, 3838–3845 (2019).
- M. E. Kleemann, R. Chikkaraddy, E. M. Alexeev, D. Kos, C. Carnegie, W. Deacon, A. C. de Pury, C. Grosse, B. de Nijs, J. Mertens, A. I. Tartakovskii, and J. J. Baumberg, "Strong-coupling of WSe₂ in ultra-compact plasmonic nanocavities at room temperature," *Nat. Commun.* **8**, 1296 (2017).

21. R. Chikkaraddy, B. de Nijs, F. Benz, S. J. Barrow, O. A. Scherman, E. Rosta, A. Demetriadou, P. Fox, O. Hess, and J. J. Baumberg, "Single-molecule strong coupling at room temperature in plasmonic nanocavities," *Nature* **535**, 127–130 (2016).
22. X. Han, K. Wang, X. Xing, M. Wang, and P. Lu, "Rabi splitting in a plasmonic nanocavity coupled to a WS₂ monolayer at room temperature," *ACS Photon.* **5**, 3970–3976 (2018).
23. D. Liu, T. Wu, Q. Zhang, X. Wang, X. Guo, Y. Su, Y. Zhu, M. Shao, H. Chen, Y. Luo, and D. Lei, "Probing the in-plane near-field enhancement limit in a plasmonic particle-on-film nanocavity with surface-enhanced Raman spectroscopy of graphene," *ACS Nano* **13**, 7644–7654 (2019).
24. J. W. Stewart, G. M. Akselrod, D. R. Smith, and M. H. Mikkelsen, "Toward multispectral imaging with colloidal metasurface pixels," *Adv. Mater.* **29**, 1602971 (2017).
25. A. W. Powell, D. M. Coles, R. A. Taylor, A. A. R. Watt, H. E. Assender, and J. M. Smith, "Plasmonic gas sensing using nanocube patch antennas," *Adv. Opt. Mater.* **4**, 634–642 (2016).
26. S. Cormier, T. Ding, V. Turek, and J. J. Baumberg, "Actuating single nano-oscillators with light," *Adv. Opt. Mater.* **6**, 1701281 (2018).
27. F. Benz, M. K. Schmidt, A. Dreismann, R. Chikkaraddy, Y. Zhang, A. Demetriadou, C. Carnegie, H. Ohadi, B. de Nijs, R. Esteban, J. Aizpurua, and J. J. Baumberg, "Single-molecule optomechanics in "picocavities"," *Science* **354**, 726–729 (2016).
28. T. B. Hoang, G. M. Akselrod, C. Argyropoulos, J. Huang, D. R. Smith, and M. H. Mikkelsen, "Ultrafast spontaneous emission source using plasmonic nanoantennas," *Nat. Commun.* **6**, 7788 (2015).
29. Y. Zhang, W. Chen, T. Fu, J. Sun, D. Zhang, Y. Li, S. Zhang, and H. Xu, "Simultaneous surface-enhanced resonant Raman and fluorescence spectroscopy of monolayer MoSe₂: determination of ultrafast decay rates in nanometer dimension," *Nano Lett.* **19**, 6284–6291 (2019).
30. K. Choi, Y. T. Lee, and S. Im, "Two-dimensional van der Waals nano-sheet devices for future electronics and photonics," *Nano Today* **11**, 626–643 (2016).
31. C. Jayasekara, M. Premaratne, S. D. Gunapala, and M. I. Stockman, "MoS₂ spaser," *J. Appl. Phys.* **119**, 133101 (2016).
32. K. F. Mak, K. He, C. Lee, G. H. Lee, J. Hone, T. F. Heinz, and J. Shan, "Tightly bound trions in monolayer MoS₂," *Nat. Mater.* **12**, 207–211 (2013).
33. K. F. Mak, C. Lee, J. Hone, J. Shan, and T. F. Heinz, "Atomically thin MoS₂: a new direct-gap semiconductor," *Phys. Rev. Lett.* **105**, 136805 (2010).
34. G. C. Li, Y. L. Zhang, and D. Y. Lei, "Hybrid plasmonic gap modes in metal film-coupled dimers and their physical origins revealed by polarization resolved dark field spectroscopy," *Nanoscale* **8**, 7119–7126 (2016).
35. Y. Meng, Q. Zhang, D. Lei, Y. Li, S. Li, Z. Liu, W. Xie, and C. W. Leung, "Plasmon-induced optical magnetism in an ultrathin metal nanosphere-based dimer-on-film nanocavity," *Laser Photon. Rev.* **14**, 2000068 (2020).
36. D. Huang, C. P. Byers, L. Y. Wang, A. L. Hoggard, B. Hoenee, S. Dominguez-Medina, S. S. Chen, W. S. Chang, C. F. Landes, and S. Link, "Photoluminescence of a plasmonic molecule," *ACS Nano* **9**, 7072–7079 (2015).
37. P. Nagpal, N. C. Lindquist, S. H. Oh, and D. J. Norris, "Ultrasoft patterned metals for plasmonics and metamaterials," *Science* **325**, 594–597 (2009).
38. F. Xiao, G. Wang, X. Gan, W. Shang, S. Cao, W. Zhu, T. Mei, M. Premaratne, and J. Zhao, "Selective excitation of a three-dimensionally oriented single plasmonic dipole," *Photon. Res.* **7**, 693–698 (2019).
39. P. B. Johnson and R. W. Christy, "Optical constants of the noble metals," *Phys. Rev. B* **6**, 4370–4379 (1972).
40. G. H. Jung, S. Yoo, and Q. H. Park, "Measuring the optical permittivity of two-dimensional materials without *a priori* knowledge of electronic transitions," *Nanophotonics* **8**, 263–270 (2019).
41. F. Xiao, W. Shang, W. Zhu, L. Han, M. Premaratne, T. Mei, and J. Zhao, "Cylindrical vector beam-excited frequency-tunable second harmonic generation in a plasmonic octamer," *Photon. Res.* **6**, 157–161 (2018).
42. C. Ciraci, A. Rose, C. Argyropoulos, and D. R. Smith, "Numerical studies of the modification of photodynamic processes by film-coupled plasmonic nanoparticles," *J. Opt. Soc. Am. B* **31**, 2601–2607 (2014).
43. C. Lee, H. Yan, L. E. Brus, T. F. Heinz, J. Hone, and S. Ryu, "Anomalous lattice vibrations of single- and few-layer MoS₂," *ACS Nano* **4**, 2695–2700 (2010).
44. J. Sun, H. Hu, D. Zheng, D. Zhang, Q. Deng, S. Zhang, and H. Xu, "Light-emitting plexciton: exploiting plasmon-exciton interaction in the intermediate coupling regime," *ACS Nano* **12**, 10393–10402 (2018).
45. J. A. Schuller, S. Karaveli, T. Schiros, K. He, S. Yang, I. Kyriassis, J. Shan, and R. Zia, "Orientation of luminescent excitons in layered nanomaterials," *Nat. Nanotechnol.* **8**, 271–276 (2013).